Pn uppermost mantle tomography of Central Tibet: Implication for mechanisms of N-S rifts and conjugate faults

Shitan Nie[a,b], Xiaobo Tian[a,c,*], Xiaofeng Liang[a,d], Yun Chen[a,d], Tao Xu[a,c]

[a] *State Key Laboratory of Lithospheric Evolution, Institute of Geology and Geophysics, Chinese Academy of Sciences, Beijing 100029, China*
[b] *University of Chinese Academy of Sciences, Beijing 100049, China*
[c] *CAS Center for Excellence in Tibetan Plateau Earth Sciences, Beijing 100101, China*
[d] *Institution of Earth Science, Chinese Academy of Science, Beijing 100029, China*

ARTICLE INFO

ABSTRACT

The north-south convergence between the Indian and Eurasian continents since Cenozoic has produced the Tibetan plateau, and east-west extension structures have also developed since late Cenozoic. Whether these extensional structures are limited to the crust or extend to the deep lithosphere remains controversial. The uppermost mantle serves as a link between the crust and deep lithosphere, the velocity structure of which provides an important constraint on exploring the mechanism of extensional structures. Based on *Pn* traveltime data recorded by the SANDWICH network in central Tibet, we use the interstation traveltime difference method to obtain the uppermost mantle velocity structure. Our results show significant velocity differences for the uppermost mantle beneath the conjugated strike-slip faults and rifts, which indicates their different formation mechanisms. The high *Pn* velocity beneath the conjugated strike-slip faults support an eastward horizontal shear at the base of the upper crust rather than the lower crust has contributed to the development of the conjugated strike-slip faults. The low *Pn* velocity beneath the rifts in Lhasa may provide evidence for the rifts cutting through the entire crust and reflect the connection between the formation of the rifts and deep tectonic activities. The most prominent features in our results are the low *Pn* velocity zones beneath the Tangra Yum Co Rift (TYR), the Pumqu-Xianza Rift (PXR) and the zone between the two rifts, and we explain the low *Pn* velocity as the top of the mantle wedge upon the subducting Indian lithospheric slab.

1. Introduction

The continental collision between the India and the Eurasia since Cenozoic has produced the Tibet Plateau. The north-south trending rifts and conjugated strike-slip faults which indicate the east-west extension was developed in central Tibet despite of the north-south compression stress environment. Whether these extensional structures are limited to the crust or cut through the entire lithosphere remains controversial. To explain the rifting mechanism, some models are proposed including gravitational collapse (England and Houseman, 1989), oblique convergence (McCaffrey and Nábělek, 1998) and Indian lower crust extrusion (Kapp and Guynn, 2004). Recently, some researchers have suggested that the formation of rifts may be related to deep dynamic processes, such as upwelling of the asthenosphere (Tian et al., 2015; Yin, 2000) and tearing of the subducted plate (Chen et al., 2015; Liang et al., 2016a). Yin and Taylor (2011) propose that conjugate strike-slip

faults are formed by the continuous convergence between the Indian and Eurasia and the eastward flow of the asthenosphere. However, the shear wave splitting results show the regionally dominant ENE-WSW oriented upper-mantle anisotropy which is inconsistent with the eastward flow of the asthenosphere material (Wu et al., 2019).

The uppermost mantle velocity structures are widely used to discuss the activity of the lithosphere and can provide key constraints on the formation mechanism of the extensional structures. Using the traveltime of *Pn* phases is the most direct and effective way to obtain the uppermost mantle velocity structure (Hearn et al., 2004). A series of *Pn* velocity studies have been carried out in Tibet (Hearn et al., 2019; Hearn et al., 2004; Lei et al., 2014; Li and Song, 2018; Liang and Song, 2006; Lü et al., 2017; McNamara et al., 1997; Pei et al., 2007; Phillips et al., 2005; Zhou and Lei, 2016). However, due to sparse seismic stations in Tibet, a high-resolution image of the uppermost mantle velocity structure is still needed in central part of the plateau.

* Corresponding author at: State Key Laboratory of Lithospheric Evolution, Institute of Geology and Geophysics, Chinese Academy of Sciences, Beijing 100029, China.
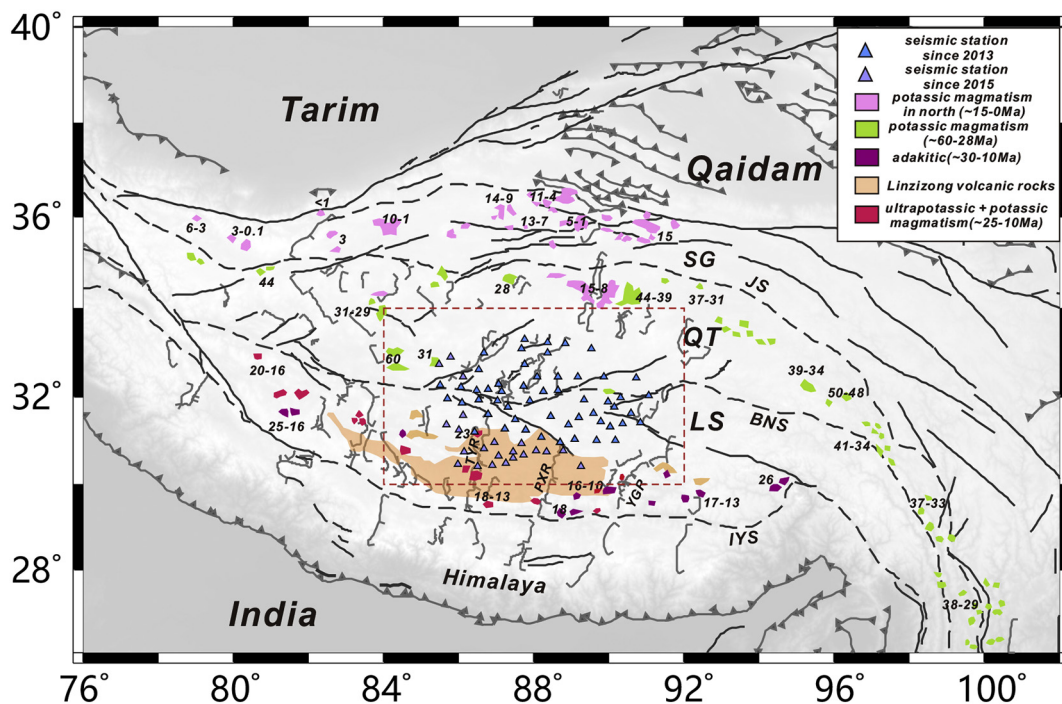*E-mail address:* txb@mail.iggcas.ac.cn (X. Tian).

Fig. 1. Tectonic(Taylor and Yin, 2009) and topography map of Tibet with the SANDWICH seismic broadband stations used in this study. The triangles display the SANDWICH seismic stations. The light blue triangles represent the initial 53 stations, and the 22 light purple triangles are the stations set up after October 2015. Filled irregular blocks mark different episodes of magmatism and the ages (Million years) are shown as the accompanying numbers (Chung et al., 2005). IYS: = Indus -Yarlung Suture, BNS: = Bangong - Nujiang Suture, JS: = Jinsha Suture, LS: = Lhasa Terrane, QT: = Qiangtang Terrane, SG: = Songpan - Ganzi Terrane, YGR: = Yadong- Gulu Rift, PXR: = Pumqu - Xianza Rift, TYR: = Tangra Yum Co Rift. (For interpretation of the references to colour in this figure legend, the reader is referred to the web version of this article.)

In this study, we apply the interstation *Pn* traveltime difference method to the records from the SANDWICH broadband seismic array (Liang et al., 2016b) in central Tibet to image high-resolution uppermost mantle velocity structures and provides key constraints for the formation mechanism of the widely distributed extensional structures in central Tibet.

2. Tectonic setting

North of the Himalayas and the Indus-Yarlung Suture, the main part of the Tibetan Plateau consists of the Lhasa, Qiangtang, and Songpan-Ganzi terranes from south to north. These three terranes are connected by the BNS and Jinsha Suture (JS) (Fig. 1). The average crustal thickness of Tibet is approximately 70 km, with the Lhasa terrane being the thickest (~ 75 km), and the Qiangtang terrane is approximately 65 km (Zhang et al., 2011). The lithosphere of Tibet, however, has not thickened significantly with an average thickness of ~140 km (Zhang et al., 2014). At present, there is considerable evidence supporting delamination of the lithosphere in central and northern Tibet, including inefficient Sn propagation (McNamara et al., 1995), low velocity of *Pn* (McNamara et al., 1997), thinning of the lithosphere (Zhang et al., 2014), thickening of the mantle transition zone (Chen et al., 2010), and the distribution of volcanic rocks (Chung et al., 2005).

The volcanic rocks of the Tibetan Plateau are distributed along the block in an east-west orientation (Fig. 1). The Lhasa terrane is distributed with ultrapotassic volcanic rocks (25–8 Ma), potassic volcanic rocks (27–8 Ma), adakites (30–15 Ma) and the Linzizong volcanic rocks (~45 Ma). The two episodes of potassic volcanic rocks in the Qiangtang terrane include the Eocene to Oligocene potassic volcanic rocks (65–28 Ma) and the Mid-Miocene to Quaternary potassic volcanic rocks (10–0 Ma). Potassium rich volcanic rocks since 10 Ma are mainly distributed in the northern Qiangtang and Songpan-Ganzi terranes (Chung et al., 2005). The Linzizong volcanic rocks are produced by tectonic

magmatism from the main collision between India and Eurasia. Two kinds of magma actions produce adakites: the subduction of oceanic crust and thickening of the lower crust. Widespread potassic volcanic rocks and ultrapotassic volcanic rocks are produced postcollision. The initial collision between India and Eurasia occurred on the west Himalaya at ~55 Ma and gradually became later from west to east (Copley et al., 2010; Lee and Lawver, 1995), which implies the subducted Indian plate may differ laterally.

The N-S trending rifts and conjugated strike-slip faults are the most prominent extensional structures in Tibet. The rifts first formed at ~20 Ma. The spatial distribution of the rifts is dense in the north and sparse in the south (Cooper et al., 2015). There are six major rifts in the Lhasa terrane from west to east, including the Yari Rift (YRR), North Lunggar Rift (NLR), Tangra Yum Co Rift (TYR), Pumqu-Xianza Rift (PXR), Yadong-Gulu Rift (YGR), and Comei Rift (CR). Several shallow mechanisms have been proposed to explain the formation of the rifts, including gravity collapse (England and Houseman, 1989), oblique convergence (Cogan et al., 1998; McCaffrey and Nábělek, 1998), and northern Tibet lateral extrusion (Tapponnier et al., 2001). However, increasing evidence supports the rift formation being related to deep processes (Hoke et al., 2000). Deep processes including a tearing slab, asthenospheric upwelling, and mantle convection have also been proposed to explain the development of the rifts (Chen et al., 2015; Hou et al., 2004; Liang et al., 2016a; Tian et al., 2015; Yin, 2000). The conjugated strike-slip faults are distribution in central Tibet (Yin and Taylor, 2011) and southeastern Tibet (Lei et al., 2012).

3. Data and methods

Our data comes from the 2-D SANDWICH broadband seismic array (Liang et al., 2016b) that began recording in November 2013 and finished in February 2017. There are 75 seismic stations in total, containing the initially deployed 53 stations (light blue triangles) and 22
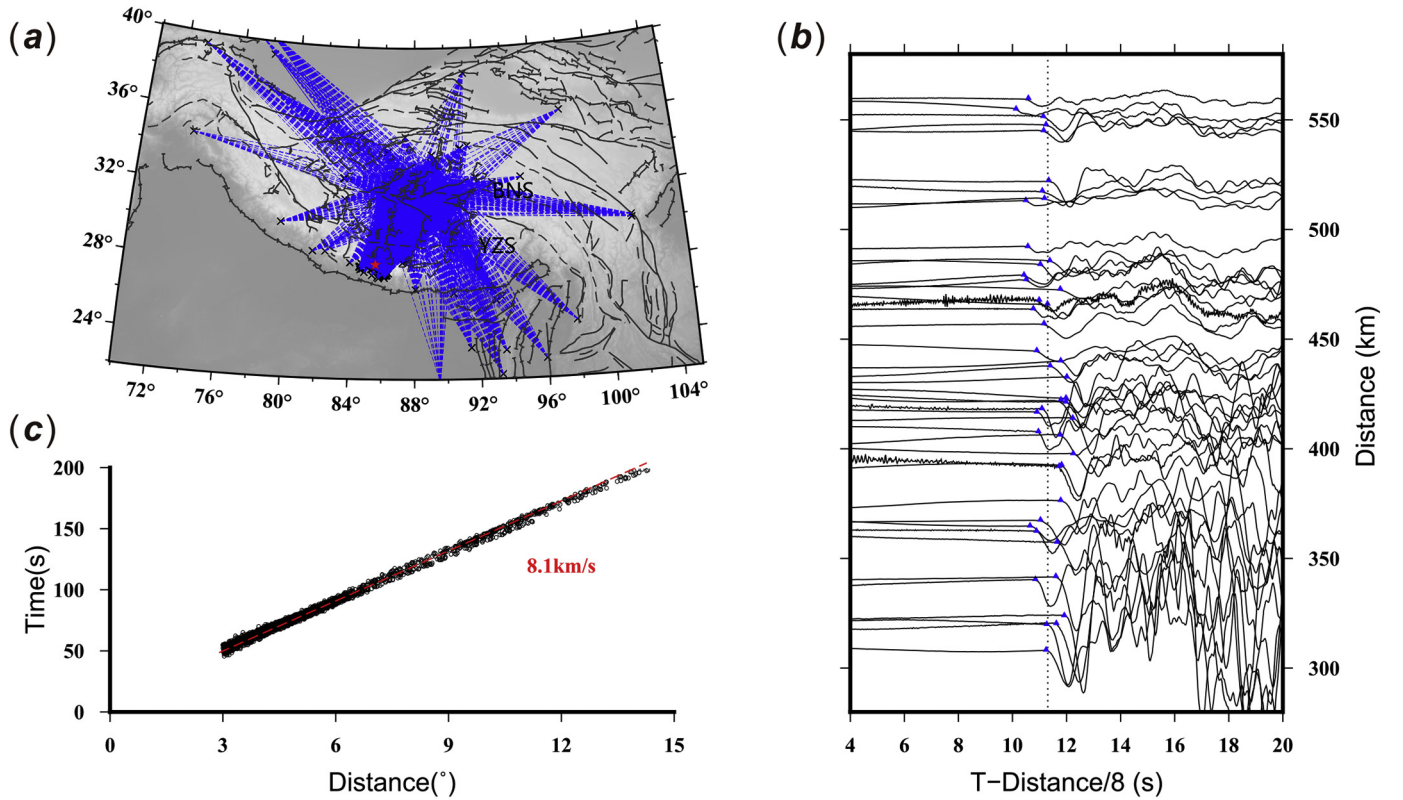
Fig. 2. (a) *Pn* ray paths measured in this study. Black crosses are earthquakes. Blue dashed lines represent the *Pn* ray paths. (b) A typical *Pn* phase waveforms recorded by the SANDWICH array. The vertical axis is the epicentral distance, and the horizontal axis is the reduced traveltime according to 8 km/s. Blue triangles mark the *Pn* arrival picked at each station. The location of the earthquake is shown in (a) by a red star. The black dashed line represents the average reduced traveltime of *Pn* arrival for this event. (c) Traveltimes for *Pn* versus epicentral distance. Average *Pn* velocity of 8.1 km/s was determined by the slope of the red line. (For interpretation of the references to colour in this figure legend, the reader is referred to the web version of this article.)

other stations (light purple triangles) set up after October 2015 (Fig. 1). The stations are distributed on both sides of the BNS from the northern Lhasa terrane to the southern Qiangtang terrane, and their spacing is approximately 40 km on average. We search for earthquake events with Ms. > 4 from the USGS (United States Geological Survey) catalog. For the very thick 70 km crust in Tibet, the *Pn* phase starts to appear at 2.5° (Liang et al., 2016b). To make sure a clear separation between *Pn* and *Pg*, we set a maximum limit for focal depth as 60 km and epicentral distances between 3 and 15 degrees are fine.

We measure *Pn* arrivals manually and obtain a total of 2400 rays from 189 earthquake events. Fig. 2a show the *Pn* ray path distribution and Fig. 2b exhibit an example of *Pn* arrival measurements from the waveforms of an earthquake event. It can be clearly seen that the phase and arrival time of the first *Pn* waveform are clear and consistent from 250 km to 600 km in Fig. 2b. Therefore, it can be confirmed from the original waveform analysis that the picked up time is a *Pn* wave. Fitting the data set of *Pn* traveltime versus epicentral distance in distance, we obtain an average *Pn* velocity of 8.1 km/s (Fig. 2c), consistent with the average uppermost mantle velocity in this region obtained by previous study (Liang and Song, 2006). Fig. S1 shows the variation of reduced *Pn* travel times versus epicentral distance for an earthquake event. The stations in the south show increasingly early traveltimes, while those stations in north show decreasingly reduced *Pn* traveltime with epicentral distance. This feature might reflect northward increasing of the *Pn* velocity or/and northward decreasing of crustal thickness.

The traditional *Pn* traveltime imaging method divides the *Pn* path into the station term, the source term and the uppermost mantle path term (Hearn et al., 2004). This method brings two parts of error into the inversion. On one hand, relatively large errors of earthquake locations and origin time, due to the scarcity of stations in Tibet, can greatly reduce the reliability of the inversion results. The analyses of

earthquake location robustness in central Tibet (Zhu et al., 2017; Zhu and Helmberger, 1996) suggest that the differences in both the epicenter and the focal depth after relocation can be as large as 10 km compared to the earthquake catalogs. The second source of errors comes from the *Pn* traveltime imaging method assumes that the crustal thickness in the circle formed by the *Pn* transition point below the station is constant, that is to say, the station delay for each station is fixed and does not change with the source back azimuth. However, the crustal thickness of the Tibetan plateau has reached 70 km causing the diameter of the circle on the Moho to reach more than 160 km, and in that case, the thickness of the crust may change by over 20 km in some areas (Zhang et al., 2011). The *Pn* phase ray path can be divided into three parts, including the downgoing part from source to Moho, the sliding part at the uppermost mantle, and the upgoing part from Moho to receiver station (Fig. 3a). We assume that the crust thickness difference on both legs is d_c, and the crustal and upper mantle velocities are 6.3 km/s (V_C) and 8.0 km/s (V_{Pn}), respectively (Fig. S2). The traveltime difference of the *Pn* path to both legs is:

$$T = \frac{d_c}{\cos\theta V_C} - \frac{d_c \tan\theta}{V_{Pn}} = \frac{\frac{d_c V_{Pn}}{V_C}}{\sqrt{V_{Pn}^2 - V_C^2}} - \frac{\frac{d_c V_C}{V_{Pn}}}{\sqrt{V_{Pn}^2 - V_C^2}} \tag{1}$$

When the thickness of the crust difference is 20 km, the traveltime difference of 1.9566 s will be attributed into the upper mantle horizontal path which will cause a great impact on the inversion result.

To achieve more reliable and higher resolution *Pn* wave velocity structure, interstation *Pn* traveltime difference tomography has been used in different regions (Li et al., 2012; Phillips et al., 2005). In this study, we adopt this inversion scheme to eliminate the influence of the source uncertainty including both earthquake location and origin time. For a *Pn* path (Fig. 3a), we use L^{eq}(source to Moho), L^{Moho}(Moho), L^{st}
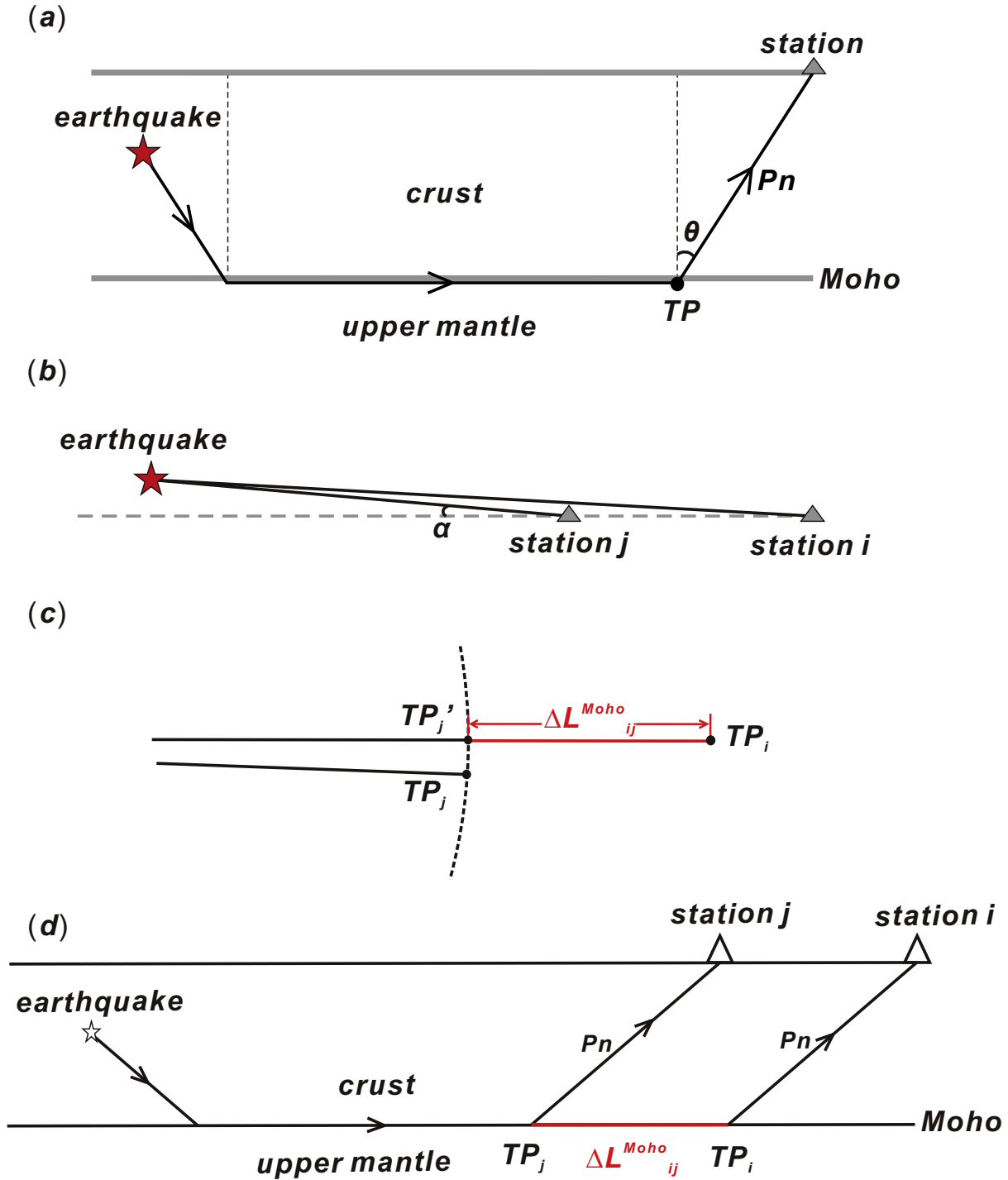
(**a**)

(**b**)

(**c**)

(**d**)

Fig. 3. Schematic of interstation traveltime differences method for *Pn* wave. (a) Theoretical ray path of a *Pn* phase. (b) Mapview of the horizontal projection of *Pn* paths from an earthquake to stations *i* and *j*. (c) Mapview for the horizontal raypath difference between two tuning points *i* and *j* of *Pn* paths from an earthquake to stations *i* and *j*. **TP$_i$** and **TP$_j$** represent the locations of turning points *i* and *j*, respectively. **TP$_j$'** represents the equidistant point of **TP$_j$** along the longer path. Straight lines are all great circle paths. (d) A sketch shows that the upper mantle interstation path (red line) can locate outside the network. (For interpretation of the references to colour in this figure legend, the reader is referred to the web version of this article.)

(Moho to receiver) denoting the lengths and T^{eq}, T^{Moho}, T^{st} denoting the traveltime of the three parts, respectively. θ represents the angle of the total reflection. Thus, the epicentral distance (*D*) and the travel time of *Pn* (*T*) are:

$$D = L^{eq} \cdot \sin\theta + L^{Moho} + L^{st} \cdot \sin\theta \qquad (2)$$

$$T = T^{eq} + T^{Moho} + T^{st} \qquad (3)$$

As illustrated in Fig. 3b, if two stations *i*, *j* receive *Pn* wave from the same earthquake and α is small, they can be considered as a station-pair. T_i^{eq} and L_i^{eq} are approximately equal to T_j^{eq} and L_j^{eq}. Hence, the *Pn* traveltime difference of the station-pair (ΔT_{ij}) and epicentral distance difference (ΔD_{ij}) can be expressed as:

$$\Delta T_{ij} = T_i^{Moho} - T_j^{Moho} + T_i^{st} - T_j^{st} = \Delta T_{ij}^{Moho} + T_i^{st} - T_j^{st} \qquad (4)$$
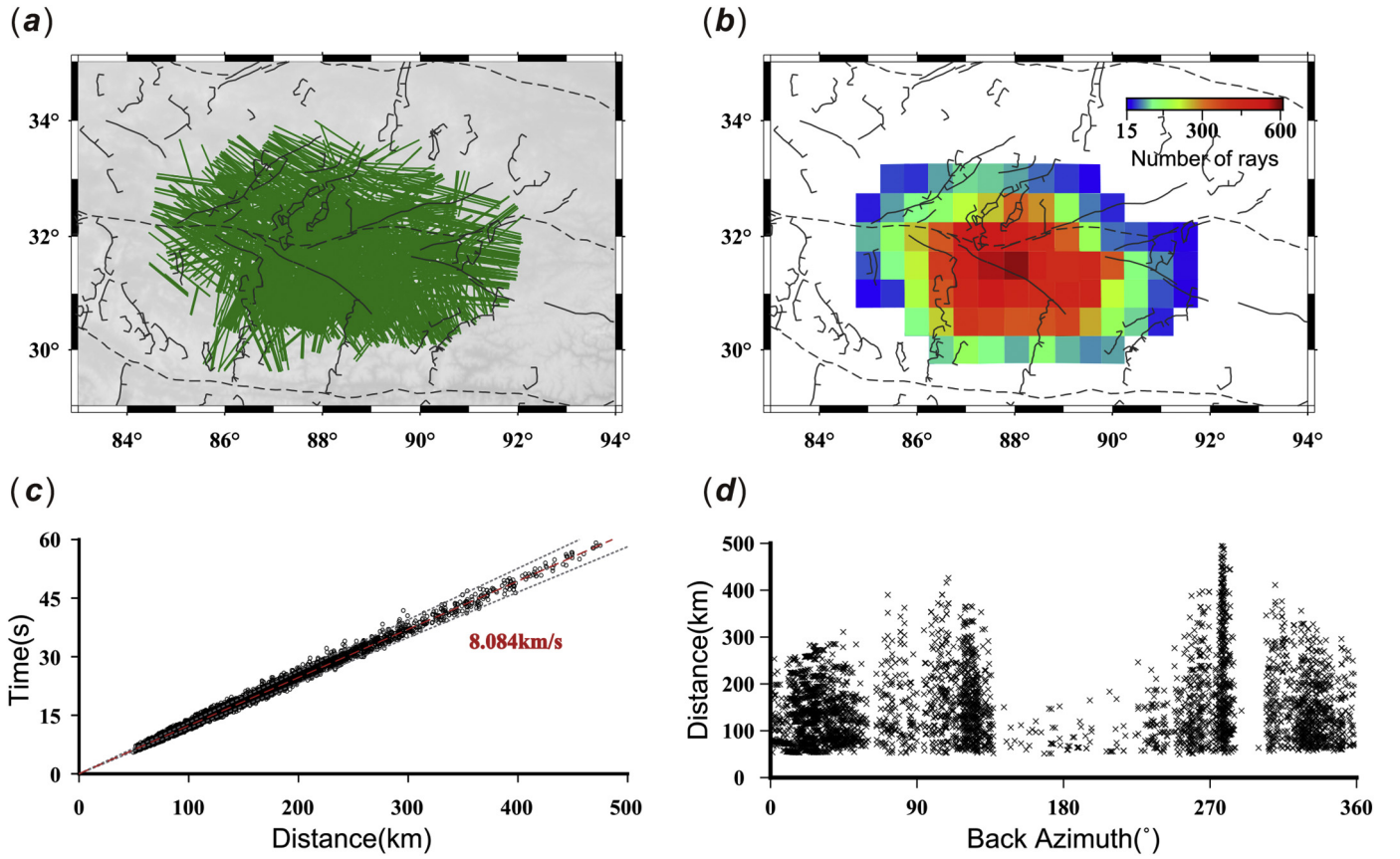
(a)

(b)

(c)

(d)

Fig. 4. Ray path and azimuth coverage for our *Pn* measurements. (a) Path coverage of *Pn* traveltime difference data used in our tomographic inversion. (b) Path density is defined as the number of rays intersecting each 0.5° × 0.5° grid. (c) Average *Pn* velocity in the study area determined by regression of *Pn* traveltime differences versus interstation distance (red dashed line). The red dashed line indicates the velocity of 8.084 km/s. Black dashed lines denote the velocities of 7.9 km/s and 8.3 km/s, respectively. (d) The differential distance versus back azimuth for different station pairs. (For interpretation of the references to colour in this figure legend, the reader is referred to the web version of this article.)

$$\Delta D_{ij} = L_i^{Moho} - L_j^{Moho} + L_i^{st} \cdot \sin\theta - L_j^{st} \cdot \sin\theta = \Delta L_{ij}^{Moho} + L_i^{st} \cdot \sin\theta - L_j^{st}$$
$$\cdot \sin\theta \tag{5}$$

Where ΔT_{ij}^{Moho} and ΔL_{ij}^{Moho} are traveltime and ray length difference at the uppermost mantle of a station-pair, respectively, and we can rearrange Eqs. (4) and (5) to yield:

$$\Delta T_{ij}^{Moho} = \Delta T_{ij} - T_i^{st} + T_j^{st} \tag{6}$$

$$\Delta L_{ij}^{Moho} = \Delta D_{ij} - L_i^{st} \cdot \sin\theta + L_j^{st} \cdot \sin\theta \tag{7}$$

L_i^{st}, L_j^{st}, T_i^{st} and T_j^{st} can be obtained using the crustal thickness and average P-wave velocity, so we can calculate the travel time ΔT_{ij}^{Moho} and length ΔL_{ij}^{Moho} of the rays in the uppermost mantle. We use a two-dimensional grid mesh to express the slowness perturbation in the uppermost mantle. $\Delta S(\varphi_i, \omega_j)$ denotes the slowness perturbation at the grid node. If there is a segment of ray path in a cell k (Fig. S3), the average slowness perturbation of this segment can be expressed as:

$$\Delta S_k(\varphi, \omega) = \sum_{i=1}^{2} \sum_{j=1}^{2} \Delta S_k(\varphi_i, \omega_j) \left[\left(1 - \left| \frac{\varphi - \varphi_i}{\varphi_2 - \varphi_1} \right| \right) \left(1 - \left| \frac{\omega - \omega_j}{\omega_2 - \omega_1} \right| \right) \right] \tag{8}$$

where φ is longitude and ω is latitude of the center point of the ray path in cell k (Fig. S3); φ_i and ω_j represent the coordinates for the four grid nodes surrounding the point (φ, ω). $(1 - |(\varphi - \varphi_i)/(\varphi_2 - \varphi_1)|)$ $(1 - |(\omega - \omega_j)/(\omega_2 - \omega_1)|)$ represents the weight coefficients for the linear interpolation in cell k. We use d_k to represent the ray length in cell k. The observation equation can be described as follows:

$$\Delta T = \sum d_k \Delta S_k \tag{9}$$

We add the parameter of crustal thickness perturbation (3 km) at each grid to reduce the impact from the approximation in the ray path and the errors in the crustal structure (crustal thickness and velocity). ΔH_{in} and ΔH_{out} are the perturbation of the crustal thickness at the beginning and end of the ray path, respectively.

$$\Delta T = \sum d_k \Delta S_k - C(\Delta H_{in} - \Delta H_{out})$$

$$\Delta T = \sum d_k \Delta S_k - \left\{ C(V_{Pn0}) + \frac{d[C(V_{Pn})]}{d(V_{Pn})} \right\} (\Delta H_{in} - \Delta H_{out})$$

$$\Delta T = \sum d_k \Delta S_k - \frac{1}{V_C \cos\theta}(\Delta H_{in} - \Delta H_{out}) \tag{10}$$

If **x** is a vector formed by the slowness perturbation of each grid, the problem can be formulated as a typical sparse linear equation system

$$\mathbf{Ax = t}$$

where **A** is a matrix corresponding to the coefficients for slowness and **t** is a vector of traveltime residuals. We use the damp LSQR algorithm (Paige and Saunders, 1982) to invert this linear system.

According to Li et al. (2012), the smaller the angle α, the less influence caused by earthquake uncertainty, but available station pairs will decrease. We have tested different α and found that when α exceeds 8 degrees in the Tibetan Plateau, the residual error will also increase significantly. So we set the angle α < 8 degrees (Fig. 3b). As a result, the errors of *Pn* traveltime differences generated by earthquake mislocation are less than 0.1 s (Li et al., 2012; Phillips et al., 2005). To reduce the impact of traveltime in the crust below the stations, we use a precise crustal thickness model of the study area (Fig. S4) and the

average crustal velocity. We found the inversion results differ slightly when testing average crustal P wave velocity ranging from 6.0 km/s to 6.5 km/s, so the average crustal velocity of the region is set as 6.3 km/s (Zhang et al., 2011). We use only these measurements with ΔL_{ij}^{Moho} greater than 50 km to ensure enough sampling path in the uppermost mantle. The traveltime residuals tend to converge after 100 iterations. Fig. S5 shows the relationship of maximum velocity perturbation and the RMS of traveltime residuals. By analyzing the curves of damping parameters, we chose an optimal damping constant of 180 at the inflection of the curve.

We finally get 4403 station-pairs, including their mantle ray paths and mantle traveltime differences. Fig. 4a and Fig. 4b show the distribution and density of these paths in our study area, respectively. Fig. 4c shows the mantle traveltime differences versus their mantle ray path lengths. The average uppermost mantle P-wave velocity of 8.084 km/s is determined from the slope of the regression line. The ray path lengths are arranged according to back azimuth to see if the distribution of their directions is uniform. As shown in Fig. 4d, except for relatively sparse directions near 180° other azimuths are all well covered. To examine our model resolution, we perform a conventional checkerboard test (Fig. 5). The study area is divided into 2-D grids of 0.5° by 0.5° along longitude and latitude. Our velocity perturbation is a sinusoidal pattern of 0.4 km/s in amplitude with respect to a background velocity of 8 km/s. Synthetic arrival times are calculated for the test model with the same ray paths as used in the real tomographic inversion. We also add a random noise of 0.1 s. The checkboard test indicates that 0.5° × 0.5° can be resolved for most of the studied region.

4. Results

Based on 0.5° grids, *Pn* velocity lateral variations are obtained by inverting the *Pn* traveltime residuals shown in Fig. 6. The results show that the average *Pn* velocity is 8.05 km/s in the study area, and the velocity is low in the south and high in the north. The area beneath the conjugated strike-slip faults zone on both sides of the BNS are featured by high *Pn* velocity. Low *Pn* velocities are distributed beneath the rifts in central Lhasa terrane and the most obvious low velocity distribution in the PXR, the area between the TYR and the PXR and beneath the YGR and the rift northeast from it. Fig. S6 shows the corrected result of the Moho depth after inversion. The standard deviation of the corrected

Moho depth is 1.02 km, indicating that the 3 km range of crust perturbation setting is sufficient for the inversion.

In order to verify that our results are measuring the uppermost mantle lid instead of the lowermost crust, we set up a model with high-speed lower crust (7.6 km/s) in the Lhasa terrane and the 6.3 km/s in other crust. A 0.0034 s^{-1} velocity gradient and a 8.1 km/s velocity at the top of the mantle are also used in the model. Then we utilized the approximate ray tracing (ART) method (Thurber, 1983) and the pseudo-bending ray tracing method (Um and Thurber, 1987) to calculate the fastest ray path between the source and the station. The results show that when the epicentral distance is 3°, all rays are from the uppermost mantle (Fig. S7), not the lower crust and the obvious change of the slope appears within 3° (Fig. S8).

Traditional *Pn* tomography method uses all paths for inversion, so the measurement depth of their results depends on the distance range of the ray used. The interstation traveltime difference method is based on the distance between station pairs. The station pairs we used are in 50-500 km and concentrated within 300 km. Therefore, according to the forward model, our measurement results should mainly reflect the velocity structure below the Moho within 40 km.

We verify the reliability of our results from four aspects. First, we compare the variation of traveltime residuals before and after inversion. Fig. 7a shows traveltime residuals (the observed traveltime minus the predicted travel time for a reference model) before the inversion. Fig. 7b shows the same as Fig. 7a but after the inversion. The traveltime residuals after the inversion converge well compared to before the inversion. Most of the traveltime residuals are less than 1 s and residual standard deviations are reduced from 0.93 s to 0.302 s after the inversion. Second, in order to verify the obvious difference of *Pn* velocity on both sides of 31.5°N, we divide the study area into two parts along north of 32°N and south of 31°N. We have selected the station pairs that only pass south of 31°N and through the area north of 32°N, respectively. The arrival time in the north is earlier than the values predicted by the velocity of 8.1 km/s, whereas the south is the opposite (Fig. S9). Third, we conducted two tests by inverting the crustal thickness only to verify whether the traveltime difference is completely caused by the depth variation of crustal thickness. One initial model is a horizontal uniform crustal model and the other initial model is an observation model shown in Fig. S3. The results of the tests show that there is still a large traveltime residual and the inversion results of Moho depth are
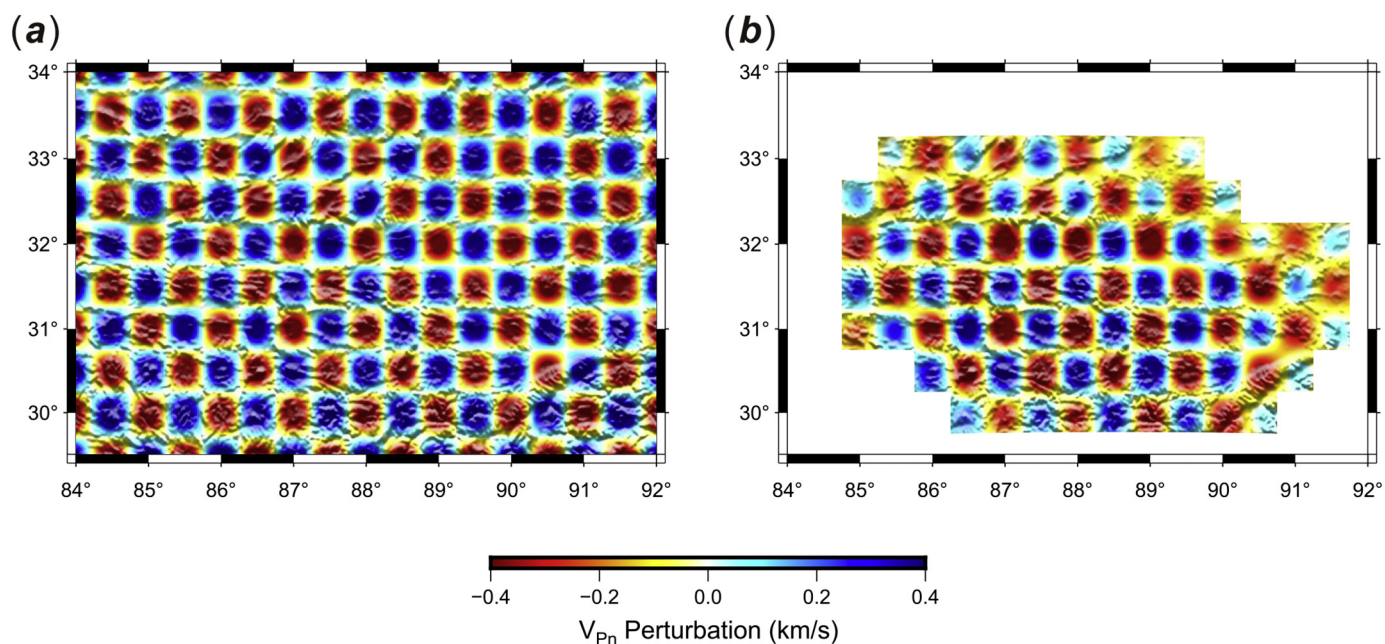

Fig. 5. Checkerboard test for our *Pn* velocity tomography. (a) and (b) are the input and output models with inversion grids spacing of 0.5° × 0.5°, respectively.
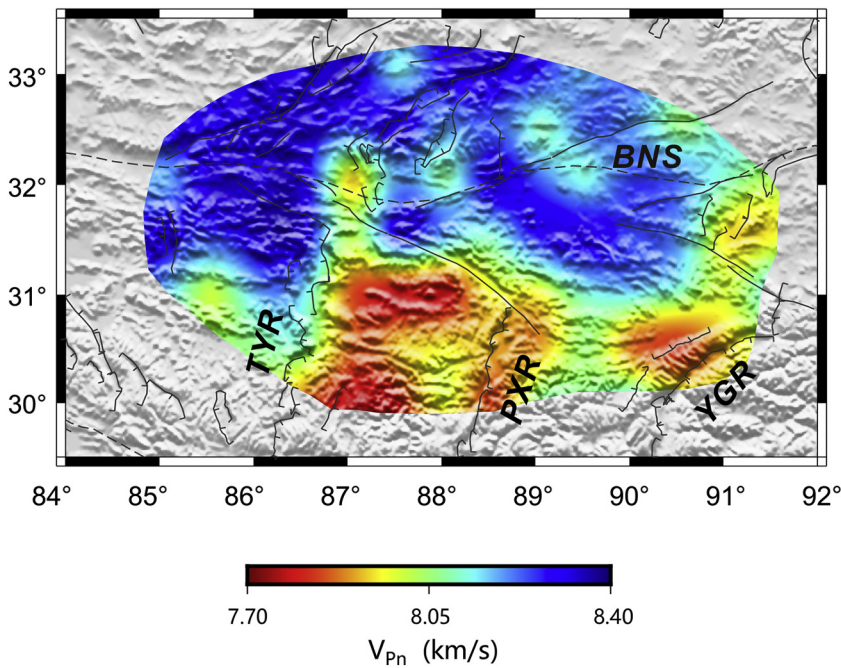
Fig. 6. *Pn* velocity map with 0.5° × 0.5° grid spacing as the tomography result. The average *Pn* velocity is 8.05 km/s. Red colour corresponds to low *Pn* velocity, and blue colour corresponds to high *Pn* velocity. The abbreviations of the geological structure are the same as Fig. 1. (For interpretation of the references to colour in this figure legend, the reader is referred to the web version of this article.)
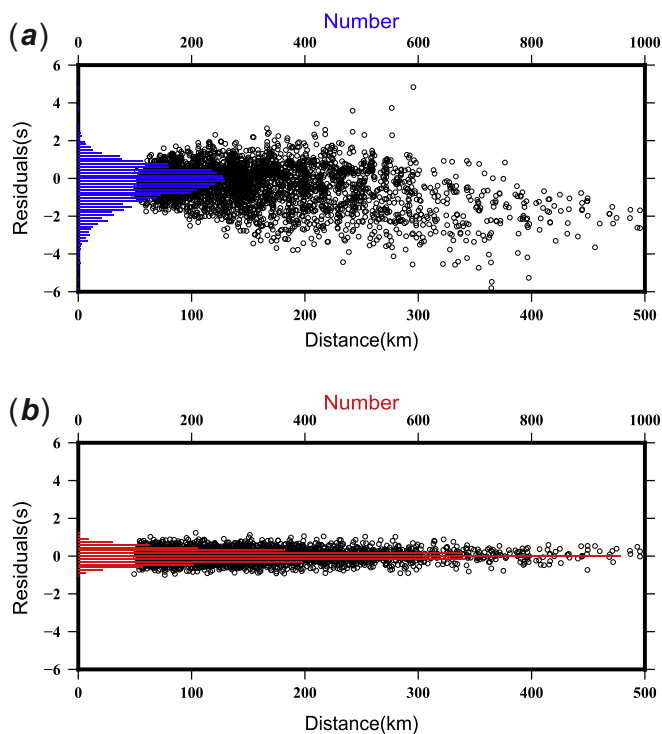

Fig. 7. Distribution of *Pn* traveltime residuals versus *Pn* traveltime difference paths (a) before and (b) after inversion. The blue and red bars show the histogram of traveltime residuals before and after inversion, respectively. The width of each bar is 0.15 s. The standard deviation of traveltime residuals decreases from 0.93 s before to 0.31 s after. (For interpretation of the references to colour in this figure legend, the reader is referred to the web version of this article.)

very different from the observed values when the *Pn* traveltime difference is only explained by the variation of crustal thickness (Fig. S10). After ruling out the possibility of explaining the *Pn* traveltime difference completely by the variations of crustal thickness alone (Fig. S10), the variation of reduced *Pn* traveltime versus epicentral distance of an earthquake event in Fig. S1 also suggests that the uppermost mantle is

featured by low and high P-wave velocity in the southern and northern parts of our study region, respectively. Finally, in order to verify whether the low velocity between the TYR and the PXR can be inverted robustly, we set a model with a connected low velocity zone (Fig. S11a) and a model with a disconnected low velocity zone (Fig. S11b) between the TYR and the PXR, respectively. There is a slight increase of *Pn* velocities between the TYR and the PXR both in the model test (Fig. S11c) and our imaging results (Fig. 6). Fig. S11d exhibits a disconnected low velocity zone that can be accurately distinguished. Therefore, it is reliable that there is a low velocity zone at the uppermost mantle between the TYR and the PXR.

We use the velocity model with low velocity in the north and high velocity in the south divided by 32°N as the input model (Fig. S12a), and the results show our ray paths can be effectively resolved (Fig. S12c). We also select the results (Liang and Song, 2006) in the same study area as the input model (Fig. S12b) and the ray paths can still be effectively resolved (Fig. S12d). Our results are different from the previous *Pn* imaging results, which may have two reasons, (1) the predecessors have fewer stations in the area, most of the rays passing through here are large distance. The result of the *Pn* wave, as the ray epicentral distance increases, reflects the velocity structure of the deeper mantle, their velocity structures may reflect the velocity of deep lithosphere and even asthenosphere (Hearn et al., 2019; Phillips et al., 2007). (2) The resolution of the predecessors in this area is 2°and the velocity structure of the uppermost mantle near the BNS may be insufficiently resolved (Hearn et al., 2004; Li and Song, 2018; Lü et al., 2017). The data we used has a good coverage of study area, so we can get a more reliable uppermost mantle structure.

5. Discussion

5.1. Comparison with previous models

The average *Pn* velocity is 8.05 km/s in the study area which has been revealed by several previous *Pn* tomographic studies. However, there are significant differences between these models. Zhou and Lei (2016) proposed low *Pn* velocity in our study area (both sides of BNS and between TYR and YGR). Pei et al. (2007) proposed that the *Pn* velocity in the entire Tibetan Plateau show normal value, except the N-S low velocity near 90°E. Liang and Song (2006) show that the area

beneath the conjugate strike-slip faults is low velocity, while the rifts to the south is high *Pn* velocity. However, Hearn et al. (2019) show that the high *Pn* velocity appears near the BNS and the low *Pn* velocity located in the area between the TYR and PXR for the 400–1000 distance range ray paths. While, for the results of 1000-1600 km ray path, the upper mantle has a low velocity north of BNS and a relatively high velocity in the south which is similar to Hearn et al. (2004). In our results, the conjugated strike-slip faults shows an obvious high *Pn* velocity and the rifts are featured by a low *Pn* velocity. The boundary between high and low speed is around 31°N. Our results are generally consistent with the results of 400-1000 km ray path from Hearn et al. (2019).

5.2. High Pn velocity beneath the conjugated strike-slip faults

The conjugate strike-slip faulting in central Tibet is basically an effect of the N-S compression from the India-Asia continental collision. Our results show that high *Pn* velocity exists on both sides of the BNS beneath conjugated strike-slip faults (the southern Qiangtang terrane and the northern Lhasa terrane). However, the high *Pn* velocities in the north of our region in the southern Qiangtang terrane are not to be confused with the well-known low velocities of the northern Qiangtang terrane (Hearn et al., 2019; McNamara et al., 1997). High P velocity in the upper mantle was also observed in previous studies using teleseismic body wave tomography (Liang et al., 2012; Tilmann et al., 2003; Wang et al., 2019). In the northern Tibetan plateau, most volcanic rocks are distributed in the northern Qiangtang terrane and are scarce in the southern Qiangtang terrane (Chung et al., 2005) (Fig. 1). Magnetotelluric observations found a distinct variation from high-conductivity upper mantle in the northern Qiangtang terrane to low-conductivity upper mantle in the southern Qiangtang terrane (Wei et al., 2001; Zeng et al., 2015). S wave receiver function results indicate the Tibetan lithosphere is not thinned approximately 32°N and 33°N (Liu et al., 2020). Triplicated phase modeling of upper mantle SH waves shows that the low velocity does not appear until deeper than 190 km in the southern Qiangtang terrane (Zhang et al., 2008). Therefore, the high *Pn* velocity in this area may indicate that the lithosphere is relatively stable and there was no widespread delamination in the late Cenozoic. We speculate that the high velocity anomaly may represent the remnant Tibetan lithosphere or Indian slab (Butterworth et al., 2014; Liang et al., 2016a; Zhu et al., 2011). Tilmann et al. (2003) suggests that the Indian continental lithospheric slab is underthrusting northward beneath Lhasa block and the leading edge has arrived the BNS. The high *Pn* velocity near the BNS in our results may be the same as the observed upper mantle high velocity exolained as the diving Indian slab (Tilmann et al., 2003) or a cold Tibetan lithosphere preserved beneath the BNS(Liang et al., 2016a). Teleseismic traveltime tomography studies (Liang et al., 2012; Tilmann et al., 2003; Wang et al., 2019) show low seismic velocity beneath south or central Lhasa block. Liang et al. (2016a) and Wang et al. (2019) suggest this part of flat Indian slab or thickening Tibetan lithosphere foundering and replaced by upwelling asthenosphere. The lithospheric foundering beneath south or central Lhasa block is aged to 25 Ma based on the magmatism study (Hao et al., 2019).

Yin and Taylor (2011) proposed that the formation of the conjugate strike-slip faults could be induced by the horizontal basal shear of the upper crust or lower crust. While, considering a dominant ENE-WSW orientation of the SKS splitting measurements (Huang et al., 2000), they preferred the horizontal basal shear of the lower crust. However, our results indicate the flow of asthenosphere cannot directly shear the lower crust due to the high *Pn* velocity beneath the conjugated strike-slip faults. Thus, we propose the horizontal shear is applied at the base of the upper crust, although the mid-lower crustal flow is not fully confirmed. Surface wave tomography, local P wave tomography, and joint inversion receiver functions and surface wave dispersion all indicate that there is a low velocity layer in the crust near the BNS, which

may be related to the formation of conjugated strike-slip faults (Xu et al., 2013; Yang et al., 2012; Zhou et al., 2019).

5.3. Low Pn velocity beneath the rifts

Low velocities in the uppermost mantle can be observed beneath rifts, such as the Reelfoot Rift (Pollitz and Mooney, 2014), the Baikal Rift (Brazier and Nyblade, 2003), the Salton trough Rift(Buehler and Shearer, 2017; Hearn, 1996) and the Shanxi Rift (Liang et al., 2004; Pei et al., 2007; Zhou and Lei, 2016). However, there are not obvious low velocity anomalies beneath the midcontinent rift near the Reelfoot Rift (Pollitz and Mooney, 2014). Our results exhibit significant low-velocity anomalies beneath the rifts in southern Tibet compared to the area beneath conjugate strike-slip faults. Receiver functions observed Moho offset beneath the TYR and the PXR (Guo et al., 2018). Virtual deep seismic sounding (Tian et al., 2015) and deep seismic sounding profiles (Zhang and Klemperer, 2005) also show Moho offset beneath the YGR and northeast of the YGR, respectively. The low velocity zones we obtained are consistent with the locations of the Moho offsets mentioned above. The result of an east-west magnetotelluric profile that passes through the YGR shows that the high-conductivity anomaly below the YGR extends from the upper crust to the upper mantle (Wang et al., 2017). Recent S-wave receiver function results suggest that Indian lithosphere plates may have larger subduction angles in western YGR than in east (Liu et al., 2020). The magmatism activities mainly located along the rifts and the observation of helium isotopic ratios from geothermal springs in southern Tibet all indicate that hot materials are upwelling from the upper mantle through the rifts (Guo et al., 2007; Hoke et al., 2000; Hou et al., 2004). The crustal velocity structure of the rifts have been studied by ambient noise tomography in southern Tibet and the low velocity range gradually increases with depth (Guo et al., 2009; Lu and Lei, 2016). These results suggest that the rifts in southern Tibet may cut through the entire crust to the upper mantle and the formation of the rifts may be related to the tectonic activity of the deep lithosphere. For example, tearing of the Indian lithospheric plates causes the upwelling of asthenosphere material along the slab window, resulting in the formation of rifts (Chen et al., 2015; Liang et al., 2016a; Tian et al., 2015).

5.4. Large dip angle of the subducting Indian slab between TYR and PXR

In addition to the north-south difference, our results show that the velocity structure also has east-west changes in central Lhasa terrane. The results of S-wave receiver function, teleseismic body wave tomography, surface wave tomography and shear wave splitting also show significant east-west variation in the subducted angle of Indian lithospheric plates (Bao et al., 2015; Chen et al., 2015; He et al., 2018; Huang and Zhao, 2006; Li et al., 2008; Wei et al., 2012; Zhao et al., 2010). In particular, the steepest dip angle exist under eastern Tibet (Lei et al., 2014; Lei et al., 2009), suggesting the existence of the big mantle wedge (Lei et al., 2019). The lowest *Pn* velocity in our results is beneath the TYR, PXR and between the two rifts. Magnetotelluric results observed pronounced low resistivity beneath the PXR in the uppermost mantle, suggesting that the mantle lithosphere is missing and that upwelling asthenospheric thermal material directly reaches the uppermost mantle (Liang et al., 2018). Deep seismic reflection profiles indicate that the Indian lithospheric plate subducts at the angle of ~27°along 88° E (Guo et al., 2017). While the receiver function results for Hi-CLIMB and the INDEPTH on both sides of the study area indicate that the Indian lithosphere subducted underplating beneath the southern Lhasa (Kind et al., 2002; Nábělek et al., 2009). Intermediate-depth earthquakes mainly distributed between 86°E ~ 89°E may also suggest steep subduction of the Indian lithosphere within this range (Monsalve et al., 2006). In subduction zones, teleseismic body wave tomography and numerical simulation all show a low velocity zone in the upper mantle above the high angle subducting plate, which may be

related to partial melting of the upper mantle caused by subducting plate dehydration (Abers et al., 2006; Zhao, 2017). We infer that the low *Pn* velocity in this region is related to the upwelling of the asthenosphere caused by the subduction of the Indian lithosphere.

6. Conclusions

The average *Pn* velocity in central Tibet is 8.05 km/s based on the interstation traveltime difference method. The uppermost mantle in the study area is characterized by high *Pn* velocity beneath the BNS, including the south Qiangtang terrane and north Lhasa terrane, with low *Pn* velocity beneath the central and south Lhasa terrane and indicate different formation mechanisms for conjugated strike-slip faults and rifts. The high *Pn* velocity in the north of our region (the south Qiangtang terrane and north Lhasa terrane) may represent the remnant Tibetan lithosphere or Indian slab and also support an eastward horizontal shear at the base of the upper crust rather than the lower crust has contributed to the development of the strike-slip faults. Our results show low *Pn* velocity beneath the rifts in southern Tibet indicating that the rifts cut through the entire crust to the upper mantle. The low *Pn* velocity between the TYR and the PXR indicates that the mantle is playing a role in rifting and the Indian plate subducted in this area. There is spatial correspondence between the tearing of the Indian lithospheric slab and the north-south trending rifts, which may indicate the deep dynamics of the rifts. For example, hot asthenospheric material upwelling through the slab "window" promotes the development of the rifts.

Supplementary data to this article can be found online at https://doi.org/10.1016/j.tecto.2020.228499.

Declaration of Competing Interest

There are no conflicts of interest to declare, and the submitted manuscript has been approved by all of the authors. All of the authors agree that Xiaobo Tian may act as the corresponding author for the paper. The work described in the manuscript is original research. This research has not been published previously and is not under consideration for publication elsewhere, in whole or in part.

Acknowledgements

References

Abers, G.A., van Keken, P.E., Kneller, E.A., Ferris, A., Stachnik, J.C., 2006. The thermal structure of subduction zones constrained by seismic imaging: Implications for slab dehydration and wedge flow. Earth Planet. Sci. Lett. 241, 387–397.

Bao, X., Song, X., Li, J., 2015. High-resolution lithospheric structure beneath Mainland China from ambient noise and earthquake surface-wave tomography. Earth Planet. Sci. Lett. 417, 132–141.

Brazier, R.A., Nyblade, A.A., 2003. Upper mantle P velocity structure beneath the Baikal Rift from modeling regional seismic data. Geophys. Res. Lett. 30, 1153.

Buehler, J.S., Shearer, P.M., 2017. Uppermost mantle seismic velocity structure beneath USArray. J. Geophys. Res. 122, 436–448.

Butterworth, N.P., Talsma, A.S., Müller, R.D., Seton, M., Bunge, H.P., Schuberth, B.S.A., Shephard, G.E., Heine, C., 2014. Geological, tomographic, kinematic and geodynamic constraints on the dynamics of sinking slabs. J. Geodyn. 73, 1–13.

Chen, W.-P., Martin, M., Tseng, T.-L., Nowack, R.L., Hung, S.-H., Huang, B.-S., 2010. Shear-wave birefringence and current configuration of converging lithosphere under Tibet. Earth Planet. Sci. Lett. 295, 297–304.

Chen, Y., Li, W., Yuan, X., Badal, J., Teng, J., 2015. Tearing of the Indian lithospheric slab beneath southern Tibet revealed by SKS-wave splitting measurements. Earth Planet. Sci. Lett. 413, 13–24.

Chung, S.-L., Chu, M.-F., Zhang, Y., Xie, Y., Lo, C.-H., Lee, T.-Y., Lan, C.-Y., Li, X., Zhang, Q., Wang, Y., 2005. Tibetan tectonic evolution inferred from spatial and temporal variations in post-collisional magmatism. Earth Sci. Rev. 68, 173–196.

Cogan, M.J., Nelson, K.D., Kidd, W.S.F., Wu, C., 1998. Shallow structure of the Yadong-Gulu rift, southern Tibet, from refraction analysis of Project INDEPTH common midpoint data. Tectonics 17, 46–61.

Cooper, F.J., Hodges, K.V., Parrish, R.R., Roberts, N.M.W., Horstwood, M.S.A., 2015. Synchronous N-S and E-W extension at the Tibet-to-Himalaya transition in NW Bhutan. Tectonics 34, 1375–1395.

Copley, A., Avouac, J.-P., Royer, J.-Y., 2010. India-Asia collision and the Cenozoic slowdown of the Indian plate: Implications for the forces driving plate motions. J. Geophys. Res. 115, B03410.

England, P., Houseman, G., 1989. Extension during continental convergence, with application to the Tbetan Plateau. J. Geophys. Res. 94, 17561–17579.

Guo, Z.F., Wilson, M., Liu, J.Q., 2007. Post-collisional adakites in South Tibet: Products of partial melting of subduction-modified lower crust. Lithos 96, 205–224.

Guo, Z., Gao, X., Yao, H., Li, J., Wang, W., 2009. Midcrustal low-velocity layer beneath the central Himalaya and southern Tibet revealed by ambient noise array tomography. Geochem. Geophys. Geosyst. 10, Q05007.

Guo, X., Li, W., Gao, R., Xu, X., Li, H., Huang, X., Ye, Z., Lu, Z., Klemperer, S.L., 2017. Nonuniform subduction of the Indian crust beneath the Himalayas. Sci. Rep. 7, 12497.

Guo, X.Y., Gao, R., Zhao, J.M., Xu, X., Lu, Z.W., Klemperer, S.L., Liu, H.B., 2018. Deep-seated lithospheric geometry in revealing collapse of the Tibetan Plateau. Earth Sci. Rev. 185, 751–762.

Hao, L.-L., Wang, Q., Wyman, D.A., Ma, L., Wang, J., Xia, X.-P., Ou, Q., 2019. First identification of postcollisional A-type magmatism in the Himalayan-Tibetan orogen. Geology 47, 187–190.

He, P., Lei, J., Yuan, X., Xu, X., Xu, Q., Liu, Z., Mi, Q., Zhou, L., 2018. Lateral Moho variations and the geometry of the Main Himalayan Thrust beneath the Nepal Himalayan orogen revealed by teleseismic receiver functions. Geophys. J. Int. 214, 1004–1017.

Hearn, T.M., 1996. Anisotropic Pn tomography in the western United States. J. Geophys. Res. 101, 8403–8414.

Hearn, T.M., Wang, S., Ni, J.F., Xu, Z., Yu, Y., Zhang, X., 2004. Uppermost mantle velocities beneath China and surrounding regions. J. Geophys. Res. 109, B11301.

Hearn, T.M., Ni, J.F., Wang, H., Sandvol, E.A., Chen, Y.J., 2019. Depth-dependent Pn velocities and configuration of Indian and Asian lithosphere beneath the Tibetan Plateau. Geophys. J. Int. 217, 179–189.

Hoke, L., Lamb, S., Hilton, D.R., Poreda, R.J., 2000. Southern limit of mantle-derived geothermal helium emissions in Tibet: implications for lithospheric structure. Earth Planet. Sci. Lett. 180, 297–308.

Hou, Z.Q., Gao, Y.F., Qu, X.M., Rui, Z.Y., Mo, X.X., 2004. Origin of adakitic intrusives generated during mid-Miocene east-west extension in southern Tibet. Earth Planet. Sci. Lett. 220, 139–155.

Huang, J., Zhao, D., 2006. High-resolution mantle tomography of China and surrounding regions. J. Geophys. Res. 111, B09305.

Huang, W.-C., Ni, J.F., Tilmann, F., Nelson, D., Guo, J., Zhao, W., Mechie, J., Kind, R., Saul, J., Rapine, R., Hearn, T.M., 2000. Seismic polarization anisotropy beneath the central Tibetan Plateau. J. Geophys. Res. 105, 27979–27989.

Kapp, P., Guynn, J.H., 2004. Indian punch rifts Tibet. Geology 32, 993–996.

Kind, R., Yuan, X., Saul, J., Nelson, D., Sobolev, S.V., Mechie, J., Zhao, W., Kosarev, G., Ni, J., Achauer, U., Jiang, M., 2002. Seismic images of crust and upper mantle beneath Tibet: Evidence for Eurasian plate subduction. Science 298, 1219–1221.

Lee, T.Y., Lawver, L.A., 1995. Cenozoic plate reconstruction of Southeast Asia. Tectonophysics 251, 85–138.

Lei, J., Zhao, D., Su, Y., 2009. Insight into the origin of the Tengchong intraplate volcano and seismotectonics in Southwest China from local and teleseismic data. J. Geophys. Res. 114, B05302.

Lei, J., Zhang, G., Xie, F., Li, Y., Su, Y., Liu, L., Ma, H., Zhang, J., 2012. Relocation of the 10 March 2011 Yingjiang, China, earthquake sequence and its tectonic implications. Earthq. Sci. 25, 103–110.

Lei, J., Li, Y., Xie, F., Teng, J., Zhang, G., Sun, C., Zha, X., 2014. Pn anisotropic tomography and dynamics under eastern Tibetan plateau. J. Geophys. Res. 119, 2174–2198.

Lei, J., Zhao, D., Xu, X., Xu, Y.-G., Du, M., 2019. Is there a big mantle wedge under eastern Tibet? Phys. Earth Planet. Inter. 292, 100–113.

Li, J., Song, X., 2018. Tearing of Indian mantle lithosphere from high-resolution seismic images and its implications for lithosphere coupling in southern Tibet. Proc. Natl. Acad. Sci. U. S. A. 115, 8296–8300.

Li, C., van der Hilst, R.D., Meltzer, A.S., Engdahl, E.R., 2008. Subduction of the Indian lithosphere beneath the Tibetan Plateau and Burma. Earth Planet. Sci. Lett. 274, 157–168.

Li, Z., Ni, S., Hao, T., Xu, Y., Roecker, S., 2012. Uppermost mantle structure of the eastern margin of the Tibetan plateau from interstation Pn traveltime difference tomography. Earth Planet. Sci. Lett. 335–336, 195–205.

Liang, C., Song, X., 2006. A low velocity belt beneath northern and eastern Tibetan Plateau from Pn tomography. Geophys. Res. Lett. 33, L22306.

Liang, C., Song, X., Huang, J., 2004. Tomographic inversion of Pn travel times in China. J. Geophys. Res. 109, B11304.

Liang, X., Sandvol, E., Chen, Y.J., Hearn, T., Ni, J., Klemperer, S., Shen, Y., Tilmann, F., 2012. A complex Tibetan upper mantle: a fragmented Indian slab and no south-verging subduction of Eurasian lithosphere. Earth Planet. Sci. Lett. 333–334,

101–111.

Liang, X., Chen, Y., Tian, X., Chen, Y.J., Ni, J., Gallegos, A., Klemperer, S.L., Wang, M., Xu, T., Sun, C., Si, S., Lan, H., Teng, J., 2016a. 3D imaging of subducting and fragmenting Indian continental lithosphere beneath southern and Central Tibet using body-wave finite-frequency tomography. Earth Planet. Sci. Lett. 443, 162–175.

Liang, X., Tian, X., Zhu, G., Wu, C., Duan, Y., Li, W., Zhou, B., Zhang, M., Yu, G., Nie, S., Wang, G., Wang, M., Wu, Z., Liu, Z., Guo, X., Zhou, X., Wei, Z., Xu, T., Zhang, X., Bai, Z., Chen, Y., Teng, J., 2016b. SANDWICH: a 2D Broadband Seismic Array in Central Tibet. Seismol. Res. Lett. 87, 864–873.

Liang, H., Jin, S., Wei, W., Gao, R., Ye, G., Zhang, L., Yin, Y., Lu, Z., 2018. Lithospheric electrical structure of the middle Lhasa terrane in the south Tibetan plateau. Tectonophysics 731-732, 95–103.

Liu, Z., Tian, X., Yuan, X., Liang, X., Chen, Y., Zhu, G., Zhang, H., Li, W., Tan, P., Zuo, S., Wu, C., Nie, S., Wang, G., Yu, G., Zhou, B., 2020. Complex structure of upper mantle beneath the Yadong-Gulu rift in Tibet revealed by S-to-P converted waves. Earth Planet. Sci. Lett. 531, 115954.

Lu, Z., Lei, J., 2016. 3-D S-wave velocity structure around the 2015 Ms 8.1 Nepal earthquake source areas and strong earthquake mechanism. Chin. J. Geophys. 59, 4529–4543.

Lü, Y., Ni, S., Chen, L., Chen, Q.-F., 2017. Pn tomography with Moho depth correction from eastern Europe to western China. J. Geophys. Res. 122, 1284–1301.

McCaffrey, R., Nábělek, J., 1998. Role of oblique convergence in the active deformation of the Himalayas and southern Tibet plateau. Geology 26, 691–694.

McNamara, D.E., Owens, T.J., Walter, W.R., 1995. Observations of regional phase propagation across the Tibetan Plateau. J. Geophys. Res. 100, 22215–22229.

McNamara, D.E., Walter, W.R., Owens, T.J., Ammon, C.J., 1997. Upper mantle velocity structure beneath the Tibetan Plateau from Pn travel time tomography. J. Geophys. Res. 102, 493–505.

Monsalve, G., Sheehan, A., Schulte-Pelkum, V., Rajaure, S., Pandey, M.R., Wu, F., 2006. Seismicity and one-dimensional velocity structure of the Himalayan collision zone: Earthquakes in the crust and upper mantle. J. Geophys. Res. 111, B10301.

Nábělek, J., Vergne, J., Sapkota, S., Kafle, B., Jiang, M., Su, H., Chen, J., Huang, B.-S., the Hi-CLIMB Team, 2009. Underplating in the Himalaya-Tibet Collision Zone Revealed by the Hi-CLIMB Experiment. Science 325, 1371–1374.

Paige, C.C., Saunders, M.A., 1982. LSQR - an algorithm for sparse linear-equations and sparse Least - squares. ACM Trans. Math. Softw. 8, 43–71.

Pei, S., Zhao, J., Sun, Y., Xu, Z., Wang, S., Liu, H., Rowe, C.A., Toksöz, M.N., Gao, X., 2007. Upper mantle seismic velocities and anisotropy in China determined through Pn and Sn tomography. J. Geophys. Res. 112, B05312.

Phillips, W.S., Begnaud, M.L., Rowe, C.A., Steck, L.K., Myers, S.C., Pasyanos, M.E., Ballard, S., 2007. Accounting for lateral variations of the upper mantle gradient in Pn tomography studies. Geophys. Res. Lett. 34, L14312.

Phillips, W.S., Rowe, C.A., Steck, L.K., 2005. The use of interstation P wave arrival time differences to account for regional path variability. Geophys. Res. Lett. 32, L11301.

Pollitz, F.F., Mooney, W.D., 2014. Seismic structure of the Central US crust and shallow upper mantle: Uniqueness of the Reelfoot Rift. Earth Planet. Sci. Lett. 402, 157–166.

Tapponnier, P., Xu, Z.Q., Roger, F., Meyer, B., Arnaud, N., Wittlinger, G., Yang, J.S., 2001. Geology - Oblique stepwise rise and growth of the Tibet plateau. Science 294, 1671–1677.

Thurber, C.H., 1983. Earthquake locations and three-dimensional crustal structure in the Coyote Lake Area, Central California. J. Geophys. Res. 88, 8226–8236.

Tian, X., Chen, Y., Tseng, T.-L., Klemperer, S.L., Thybo, H., Liu, Z., Xu, T., Liang, X., Bai, Z., Zhang, X., Si, S., Sun, C., Lan, H., Wang, E., Teng, J., 2015. Weakly coupled lithospheric extension in southern Tibet. Earth Planet. Sci. Lett. 430, 171–177.

Tilmann, F., Ni, J., INDEPTH III Seismic Team, 2003. Seismic Imaging of the Downwelling Indian Lithosphere Beneath Central Tibet. Science 300, 1424–1427.

Um, J., Thurber, C., 1987. A fast algorithm for two-point seismic ray tracing. Bull. Seismol. Soc. Am. 77, 972–986.

Wang, G., Wei, W., Ye, G., Jin, S., Jing, J., Zhang, L., Dong, H., Xie, C., Omisore, B.O.,

Guo, Z., 2017. 3-D electrical structure across the Yadong-Gulu rift revealed by magnetotelluric data: New insights on the extension of the upper crust and the geometry of the underthrusting Indian lithospheric slab in southern Tibet. Earth Planet. Sci. Lett. 474, 172–179.

Wang, Z., Zhao, D., Gao, R., Hua, Y., 2019. Complex subduction beneath the Tibetan plateau: A slab warping model. Phys. Earth Planet. Inter. 292, 42–54.

Wei, W.B., Unsworth, M., Jones, A., Booker, J., Tan, H.D., Nelson, D., Chen, L.S., Li, S.H., Solon, K., Bedrosian, P., Jin, S., Deng, M., Ledo, J., Ray, D., Roberts, B., 2001. Detection of widespread fluids in the Tibetan crust by magnetotelluric studies. Science 292, 716–718.

Wei, W., Xu, J., Zhao, D., Shi, Y., 2012. East Asia mantle tomography: New insight into plate subduction and intraplate volcanism. J. Asian Earth Sci. 60, 88–103.

Wu, C., Tian, X., Xu, T., Liang, X., Chen, Y., Taylor, M., Badal, J., Bai, Z., Duan, Y., Yu, G., Teng, J., 2019. Deformation of crust and upper mantle in Central Tibet caused by the northward subduction and slab tearing of the Indian lithosphere: New evidence based on shear wave splitting measurements. Earth Planet. Sci. Lett. 514, 75–83.

Xu, Z.J., Song, X., Zhu, L., 2013. Crustal and uppermost mantle S velocity structure under Hi-CLIMB seismic array in central Tibetan Plateau from joint inversion of surface wave dispersion and receiver function data. Tectonophysics 584, 209–220.

Yang, Y., Ritzwoller, M.H., Zheng, Y., Shen, W., Levshin, A.L., Xie, Z., 2012. A synoptic view of the distribution and connectivity of the mid-crustal low velocity zone beneath Tibet. J. Geophys. Res. 117, B04303.

Yin, A., 2000. Mode of Cenozoic east-west extension in Tibet suggesting a common origin of rifts in Asia during the Indo-Asian collision. J. Geophys. Res. 105, 21745–21759.

Yin, A., Taylor, M.H., 2011. Mechanics of V-shaped conjugate strike-slip faults and the corresponding continuum mode of continental deformation. Geol. Soc. Am. Bull. 123, 1798–1821.

Zeng, S., Hu, X., Li, J., Xu, S., Fang, H., Cai, J., 2015. Detection of the deep crustal structure of the Qiangtang terrane using magnetotelluric imaging. Tectonophysics 661, 180–189.

Zhang, Z., Deng, Y., Teng, J., Wang, C., Gao, R., Chen, Y., Fan, W., 2011. An overview of the crustal structure of the Tibetan plateau after 35 years of deep seismic soundings. J. Asian Earth Sci. 40, 977–989.

Zhang, Z., Klemperer, S.L., 2005. West-east variation in crustal thickness in northern Lhasa block, Central Tibet, from deep seismic sounding data. J. Geophys. Res. 110, B09403.

Zhang, R., Wu, Q., Li, Y., Zeng, R., 2008. Upper mantle SH velocity structure beneath Qiangtang Terrane by modeling triplicated phases. Sci. Bull. 53, 3211–3218.

Zhang, X., Teng, J., Sun, R., Romanelli, F., Zhang, Z., Panza, G.F., 2014. Structural model of the lithosphere–asthenosphere system beneath the Qinghai–Tibet Plateau and its adjacent areas. Tectonophysics 634, 208–226.

Zhao, D., 2017. Big mantle wedge, anisotropy, slabs and earthquakes beneath the Japan Sea. Phys. Earth Planet. Inter. 270, 9–28.

Zhao, J., Yuan, X., Liu, H., Kumar, P., Pei, S., Kind, R., Zhang, Z., Teng, J., Ding, L., Gao, X., Xu, Q., Wang, W., 2010. The boundary between the Indian and Asian tectonic plates below Tibet. Proc. Natl. Acad. Sci. U. S. A. 107, 11229–11233.

Zhou, Z., Lei, J., 2016. Pn anisotropic tomography and mantle dynamics beneath China. Phys. Earth Planet. Inter. 257, 193–204.

Zhou, B., Liang, X., Lin, G., Tian, X., Zhu, G., Mechie, J., Teng, J., 2019. Upper Crustal Weak Zone in Central Tibet: An Implication from Three-Dimensional Seismic Velocity and Attenuation Tomography Results. J. Geophys. Res. 124, 4654–4672.

Zhu, L., Helmberger, D.V., 1996. Intermediate depth earthquakes beneath the India-Tibet Collision Zone. Geophys. Res. Lett. 23, 435–438.

Zhu, D.-C., Zhao, Z.-D., Niu, Y., Mo, X.-X., Chung, S.-L., Hou, Z.-Q., Wang, L.-Q., Wu, F.-Y., 2011. The Lhasa Terrane: Record of a microcontinent and its histories of drift and growth. Earth Planet. Sci. Lett. 301, 241–255.

Zhu, G., Liang, X., Tian, X., Yang, H., Wu, C., Duan, Y., Li, W., Zhou, B., 2017. Analysis of the seismicity in Central Tibet based on the SANDWICH network and its tectonic implications. Tectonophysics 702, 1–7.